JACS
JOURNAL OF THE AMERICAN CHEMICAL SOCIETY
pubs.acs.org/JACS
Article

Control of Hot Carrier Cooling in Lead Halide Perovskites by Point Defects

Zhaobo Zhou, Junjie He, Thomas Frauenheim,* Oleg V. Prezhdo,* and Jinlan Wang*

Cite This: J. Am. Chem. Soc. 2022, 144, 18126−18134
Read Online

ABSTRACT: Hot carriers (HCs) in lead halide perovskites are prone to rapidly relax at the band edge and waste plentiful photon energy, severely limiting their conversion efficiency as HC photovoltaic devices. Here, the HC cooling dynamics of $MAPbI_3$ perovskite with common vacancy point defects (e.g., MA_v^+ and I_v^-) and an interstitial point defect (e.g., I_i^-) is elucidated, and the underlying physics is explicated using ab initio nonadiabatic molecular dynamics. Contrary to vacancy point defects, the interstitial point defect reduces the band degeneracy, decreases the HC −phonon interaction, weakens the nonadiabatic coupling, and ultimately slows down hot electron cooling by a factor of 1.5−2. Furthermore, the band-by-band relaxation pathway and direct relaxation pathway are uncovered for hot electron cooling and hot hole cooling, respectively, explaining why hot electrons can store more energy than hot holes during the cooling process. Besides, oxygen molecules interacting with I_i^- sharply accelerate the hot electron cooling, making it even faster than that of the pristine system and revealing the detrimental effect of oxygen on HC cooling. This work provides significant insights into the defect-dependent HC cooling dynamics and suggests a new strategy to design high-efficiency HC photovoltaic devices.

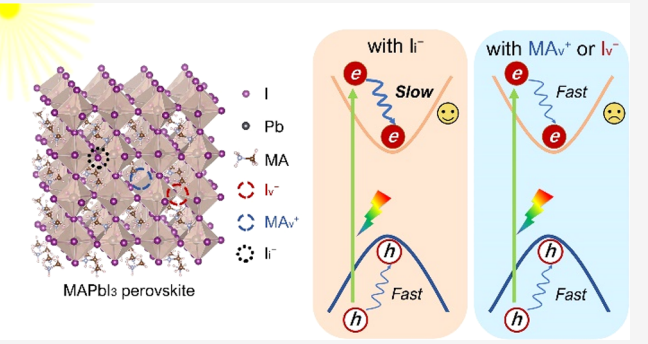

INTRODUCTION

Hybrid lead halide perovskites (LHPs) are thrust into the limelight of solar cells due to the phenomenal rise in their photovoltaic efficiencies. This advance is driven by the unique combination of perovskite's optoelectronic properties such as high optical absorption coefficient,[1] long diffusion length and carrier lifetime,[2,3] as well as defect tolerance.[4] However, further improvements to the power conversion efficiency (PCE) of perovskite solar cells have been sluggish. The certified highest efficiency is only surpassing 25%,[5] which is still below the Shockley−Queisser thermodynamic limit of ∼33% for a single-junction device.[6] The remaining photon energy is always lost via various ways. In particular, the excess energy carried by hot carriers (HCs) is dissipated to heat and cannot be utilized effectively. The underlying origin is that the HC cooling is usually much faster than the charge extraction at the contact. In theory, the PCE of solar cells can be much higher and even reach around 66% under 1 sun AM 1.5 illumination if this energy loss is mitigated.[7,8] Establishing how to slow down HC cooling in LHPs and elucidating the fundamental mechanism of this process are thus of great importance for exploring novel perovskite solar cells.

Since the first report of HC cooling in $CH_3NH_3PbI_3$ ($MAPbI_3$) polycrystalline thin films,[9] a series of impressive advances in slowing down HC cooling of LHPs have been reported.[10−15] For instance, Li et al. successfully slowed down the cooling by 2 orders of magnitude in $MAPbBr_3$ nanocrystals (∼30 ps) at high pump fluence and demonstrated efficient (≈83%) extraction of HC with an energy-selective organic layer.[16] Wang et al. demonstrated that addition of alkali cations (Cs^+, Rb^+, and K^+) in $(MAFA)Pb(BrI)_3$ markedly slowed down HC relaxation over 10 ps time scale and enhanced transport over a 100 nm length scale.[17] Yin et al. proposed that the Rashba band splitting induced by controlling organic ligands in two-dimensional Dion−Jacobson perovskites can effectively slow down HC cooling.[15] To better understand these novel experimental phenomena, various well-accepted origins and mechanisms have been discussed, such as the formation of large polarons,[18−20] hot phonon bottleneck,[21] Auger heating,[22,23] and the Rashba band splitting effect.[15] Although success has been achieved in exploring size-,[16] cation-,[10,24] and excitation intensity-dependent[25,26] slowing down of the HC relaxation and efficient HC extraction, the role of intrinsic point defects, especially their impact on HC cooling dynamics, has not been studied in detail sufficiently.

Received: August 10, 2022
Published: September 20, 2022

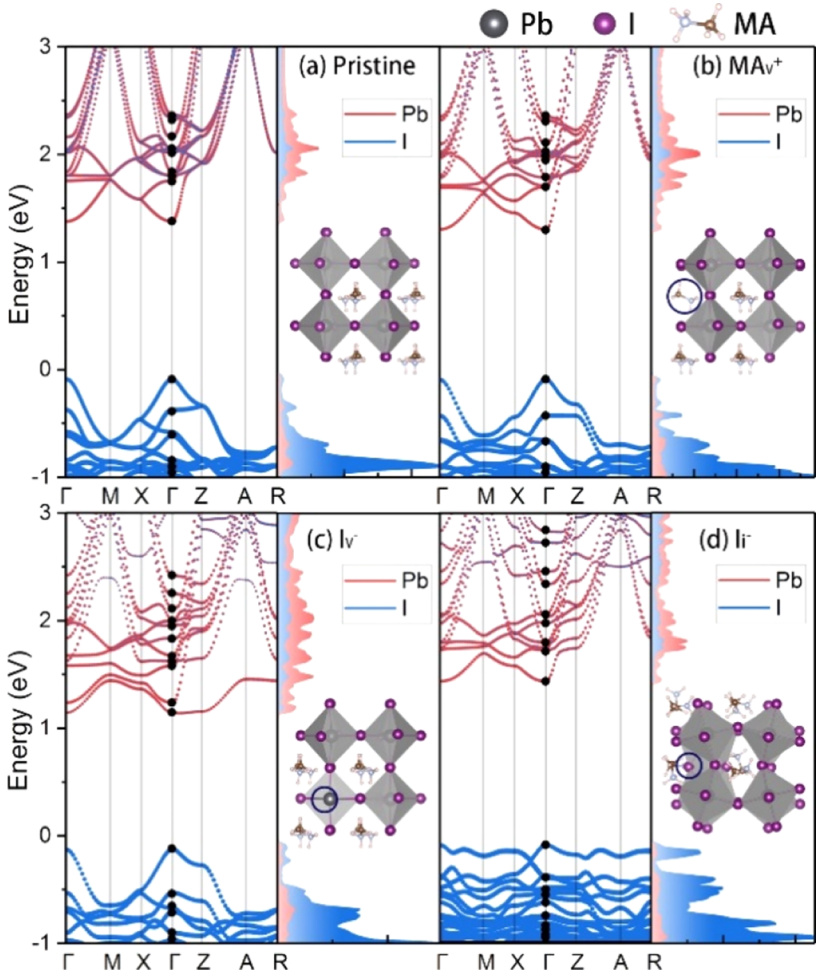

Figure 1. Band structure of pristine and defective $MAPbI_3$: (a) pristine, (b) MA_v^+, (c) I_v^-, and (d) I_i^-. The black dots show the key energy levels at the Γ point during HC relaxation. The insets show the corresponding optimized structures, and the circles indicate the defect location.

Intrinsic point defects are unavoidable in solution-processed LHPs, which have been a widespread concern in recent years. The defects are believed to be caused by structural instability in the case of exposure to light, heat, and humidity.[27] Numerous experiments have demonstrated the positive and negative effects of intrinsic point defects on the photovoltaic performance of LHPs, and the commonly accepted mechanisms have been uncovered theoretically as well.[28−35] Some vacancies (e.g., MA_v, I_v, and Pb_v) and interstitial (e.g., I_i and MA_i) defects possess relatively shallow defect states in $MAPbI_3$ and hence are electronically benign when carrier recombination is concerned.[36] The deep defect states induced by antisite defects (e.g., I_{MA}, I_{Pb}, and Pb_I) form the carrier recombination center in the band gap and consequently reduce the PCE via the Shockley−Read−Hall recombination process.[37] Different from the carrier recombination, HC cooling shows more complicated nonradiative relaxation. HCs can relax through various pathways due to the intricate distribution of band levels. Meanwhile, various interactions, for example, electron−optical phonon scatting (Fröhlich interactions), polaron interaction, carrier−acoustic phonon interaction, and carrier−carrier interaction and scatting, can contribute to the HC cooling processes.[38−42] Thus, exploring the defect-dependent HC cooling and understanding the fundamental physics behind the HC cooling dynamics in LHPs are critical to realizing their applications in new photovoltaic devices, for example, HC solar cells.

In this work, we perform first-principles calculations and ab initio nonadiabatic molecular dynamics (NAMD) simulations to elucidate the HC cooling dynamics in pristine $MAPbI_3$ and in $MAPbI_3$ containing three common point defects: MA cation vacancy (MA_v^+), iodine anion vacancy (I_v^-), and iodine anion interstitial (I_i^-). The simulations show that I_i^- reduces the band degeneracy, enlarges the energy difference between energy levels in the conduction band (CB), decreases the nonadiabatic coupling (NAC), and thus efficiently slows down the hot electron cooling by a factor of 1.5−2 within an excess energy (ΔE) of ∼0.5 eV compared to pristine $MAPbI_3$. Meanwhile, hot hole cooling has no obvious acceleration in the I_i^- system in spite of the negative effect of dense energy levels in the valence band (VB). This can be attributed to the decisive impact of weak HC−phonon interaction induced by the $[PbI_6]^{4-}$ octahedron. In addition, we observe that a hot electron exhibits a slower cooling compared with that of a hot hole for $MAPbI_3$ with and without point defects. The difference is rationalized by the fact that hot electron cooling proceeds through band-by-band relaxation, instead of direct relaxation seen in the hot hole cooling process. Meanwhile, oxygen molecules interacting with I_i^- significantly accelerate the hot electron cooling, revealing the detrimental effect of oxygen on hot electron lifetime. These results indicate that the

https://doi.org/10.1021/jacs.2c08487
J. Am. Chem. Soc. 2022, 144, 18126−18134

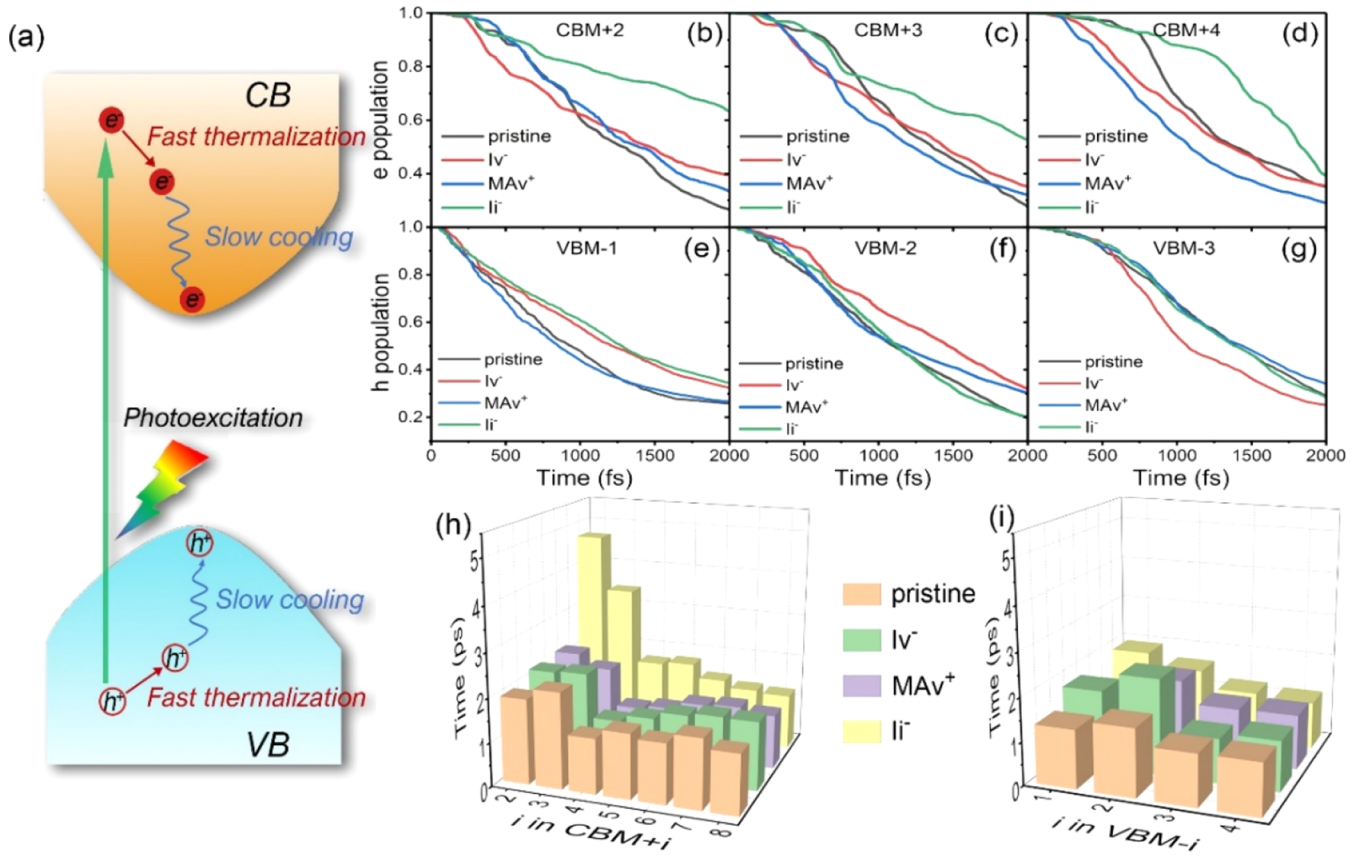

Figure 2. (a) Schematic diagram of HC relaxation processes in LHPs. (b–g) Time evolution of state population of HC relaxation in pristine and defective $MAPbI_3$. (h,i) HC relaxation times of pristine and defective $MAPbI_3$. Hot electron cooling in the I_i^- system is slowed down below CBM + 5, while hot hole cooling is similar in the pristine, MA_v^+, and I_v^- systems.

synthesis of perovskite materials should be carefully controlled to promote the formation of iodine interstitial defects and avoid the presence of oxygen, aiming to develop high-efficiency perovskite solar cells.

RESULTS AND DISCUSSION

Before evaluating the dynamics of HC cooling, it is instructive to investigate the electronic structure of pristine and various defective perovskite systems. Previous work has shown that MA_v^+, I_v^-, and I_i^- have relatively lower formation energies among vacancy and interstitial point defects, respectively, and thus are abundant during synthesis.[36] As a result, we focus our study on these three common intrinsic point defects, as illustrated in Figure 1. We observe that the CB and VB are mainly contributed by Pb orbitals and I orbitals, respectively, for the four perovskite systems. Since the MA cation and the Pb–I lattice have a weak electrostatic interaction instead of chemical bonding, introducing MA_v^+ has no apparent impact on the band structure in comparison to pristine $MAPbI_3$. However, I_v^- and I_i^- reduce the band degeneracy and increase the energy gap between each band in the CB. An explanation for this variation can be found in defect-induced changes in the Pb–I bond length and bond angle, which modulate the orbital energy levels of Pb and I. Furthermore, I_i^- significantly increases the density of states and narrows the energy gap between energy levels in the VB. Due to the excess iodine anion, on the one hand, it introduces more electrons into the bonding between Pb and I, and on the other hand, it causes a slight distortion of the $[PbI_6]^{4-}$ octahedron, which effectively localizes the spatial distribution of VB (see the inset panel of Figure 1d). A similar phenomenon also appears in excess alkali metal-doped $FAPbI_3$ perovskite.[43] In that case, we believe that the HC cooling dynamics processes will be significantly affected by point defects as well. Considering the energy range of sunlight (1.6–3.1 eV) and the band gap of the four perovskite systems (~1.5 eV), we take the energy levels of CBM + i (i = 2–8) and VBM − j (j = 1–4) at the Γ point as examples to simulate the HC cooling processes.

HCs with excess energies ΔE are created by solar irradiation when photons possess energy greater than the semiconductor band gap. These HCs then rapidly relax at the band edge by losing their excess energies to phonons (i.e., as heat) via various quantum interactions. The overall HC relaxation process can be divided into two parts: carrier thermalization and HC cooling. The former process usually occurs much faster than the latter one.[38,39] The HC relaxation dynamics starting at CBM + i (i = 2–8) and VBM − j (j = 1–4) for the four perovskite systems is depicted in Figures 2b–g and S1, respectively. The corresponding HC relaxation times are obtained by fitting with $f(t) = \exp(-t/\tau)$ and are shown in Figure 2h,i. We observe that the hot electron (hole) relaxation time depends on the initial energy. The relaxation is faster for higher initial energies, above CBM + 5 (below VBM − 3), than lower initial energies, below CBM + 5 (above VBM − 3). These results yield good agreement with two basic photophysical processes of HC cooling in LHPs. Nevertheless, since multiparticle interactions are not taken into account in this work, carrier thermalization through carrier–carrier scattering

https://doi.org/10.1021/jacs.2c08487
J. Am. Chem. Soc. 2022, 144, 18126–18134

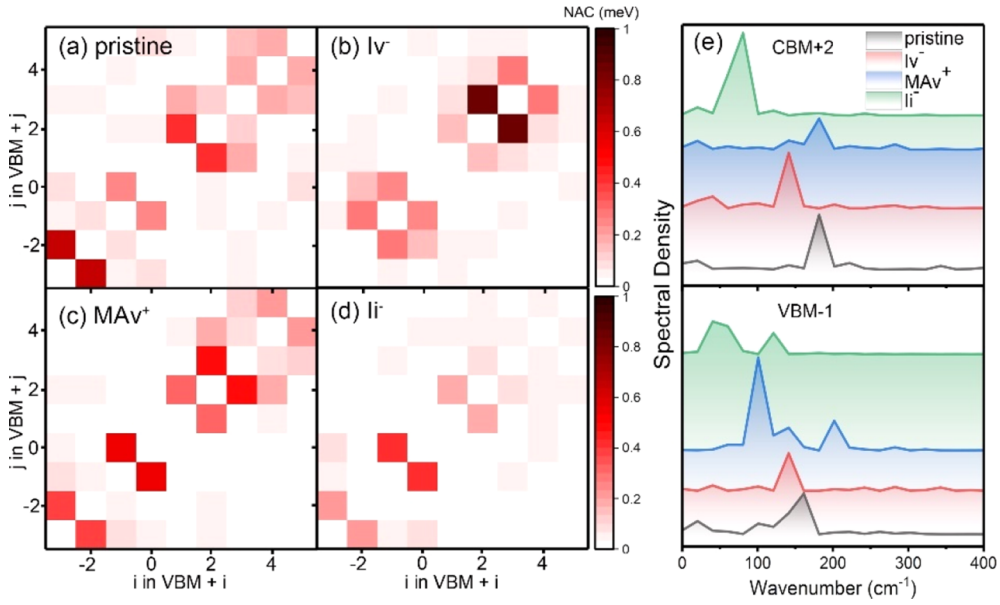

Figure 3. (a–d) Averaged absolute NACs between energy levels ranging from VBM − 3 to CBM + 5 for pristine, I_v^-, MA_v^+, and I_i^- perovskites, respectively. (e) Spectral densities of four perovskite systems at CBM + 2 and VBM − 1.

cannot be accurately described. More advanced NA–MD techniques are required for this purpose.[44−47] Thus, the HC cooling below CBM + 5 (above VBM − 3) is taken into account in the following discussion (Figure 2a). Considering the impact of defects, only I_i^- shows outstanding performance in slowing down the hot electron cooling before CBM + 5 ($\Delta E \approx 0.54$ eV) compared with MA_v^+ and I_v^-. The cooling time (~4.6 ps) at CBM + 2 ($\Delta E \approx 0.31$ eV) reaches the maximum value, twice longer than that (~1.9 ps) of the pristine system, revealing the positive effect of I_i^- in slowing down the HC cooling of LHPs. Such dynamics results are consistent with the hypothesis that increased energy gaps in the CB favor slower hot electron relaxation. Note that the hot hole cooling in the I_i^- system is similar to that in the pristine, MA_v^+, and I_v^- systems, occurring within 2 ps, even if its energy level distribution in VB is denser (Figure 1d). This implies that HC cooling dynamics cannot be determined by judging the defect-induced energy level distribution in CB and VB and that other factors should also be considered. Previous works have demonstrated that defects in LHPs will affect both electronic structure and electron–phonon scatting, revealing various novel photoexcited carrier dynamics processes.[48−50] Thus, a detailed underlying physics of defect-dependent HC cooling should be further discussed.

To further reveal the factors contributing to the HC cooling dynamics in the considered perovskite systems, we calculate the averaged absolute values of the NAC matrix elements between different states involved in the HC cooling process, as shown in Figure 3a–d. As has been discussed in the previous works,[13,24,51] the HC cooling rate is explicitly dependent on the NAC, which can be expressed as

$$d_{jk} = \left\langle \varphi_j \left| \frac{\partial}{\partial t} \right| \varphi_k \right\rangle = \frac{\langle \varphi_j | \nabla_R H | \varphi_k \rangle}{\varepsilon_k - \varepsilon_j} \dot{R} \quad (1)$$

Here, H is the Kohn–Sham Hamiltonian, φ and ε are the wave function and eigenvalue, respectively, $\dot{R}$ is the velocity of nucleus, and k and j represent different electronic states.[52] Generally, the smaller the NAC, the slower the HC cooling. It can be seen that hot electron cooling has smaller NAC values in the I_i^- system as compared with the pristine, MA_v^+, and I_v^- systems. The difference rationalizes why hot electron cooling is only suppressed in the I_i^- system, as inferred from Figure 2h. Note that the NAC values for hot hole cooling in the I_i^- system are similar to those of other considered perovskites despite the small energy gaps between energy levels (Figure 1d), suggesting that the energy gap is not the dominant factor in controlling hot hole cooling. According to formula 1, the NAC value depends on the energy difference $\varepsilon_k - \varepsilon_j$, the electron–phonon (e–ph) coupling term $\langle \varphi_j | \nabla_R H | \varphi_k \rangle$, and the nuclear velocity term $\dot{R}$. Thus, we hypothesize that some other potential factors can determine the HC cooling dynamics, for example, e–ph interaction induced by lattice thermal fluctuation. In general, the effects of lattice thermal fluctuations among different systems can be assessed by comparing the frequencies of the phonon mode participating in the excited-state dynamics process. The lower the frequency of the phonon mode, the slower the atomic fluctuations, and the smaller the $\dot{R}$ vector in NAC. Besides, quantum decoherence can also play an important role in charge carrier dynamics since quantum decoherence takes place on a time scale ranging from a few femtoseconds to hundreds of femtoseconds, which is much faster than quantum transition, leading to carrier recombination and exciton annihilation, occurring within hundreds of picoseconds to nanoseconds. However, in this work, the decoherence effect can be ignored owing to the rapid cooling along the quasi-continuous manifold of excited electronic states.[53,54]

For further understanding of carrier interaction with lattice thermal fluctuations and their effect on HC cooling processes, we take CBM + 2 and VBM − 1 levels as examples and plot their Fourier transform spectra in the four perovskite systems, Figure 3e. The peaks around and below 100 cm^{-1}, at 130–170 cm^{-1}, and around 200 cm^{-1} can be attributed to the I–Pb stretching and bending motions, organic cation librations, and torsion, respectively.[55,56] In Figure 3e, the dominant peak in hot electron cooling of the I_i^- system shows a lower frequency

https://doi.org/10.1021/jacs.2c08487
J. Am. Chem. Soc. 2022, 144, 18126−18134

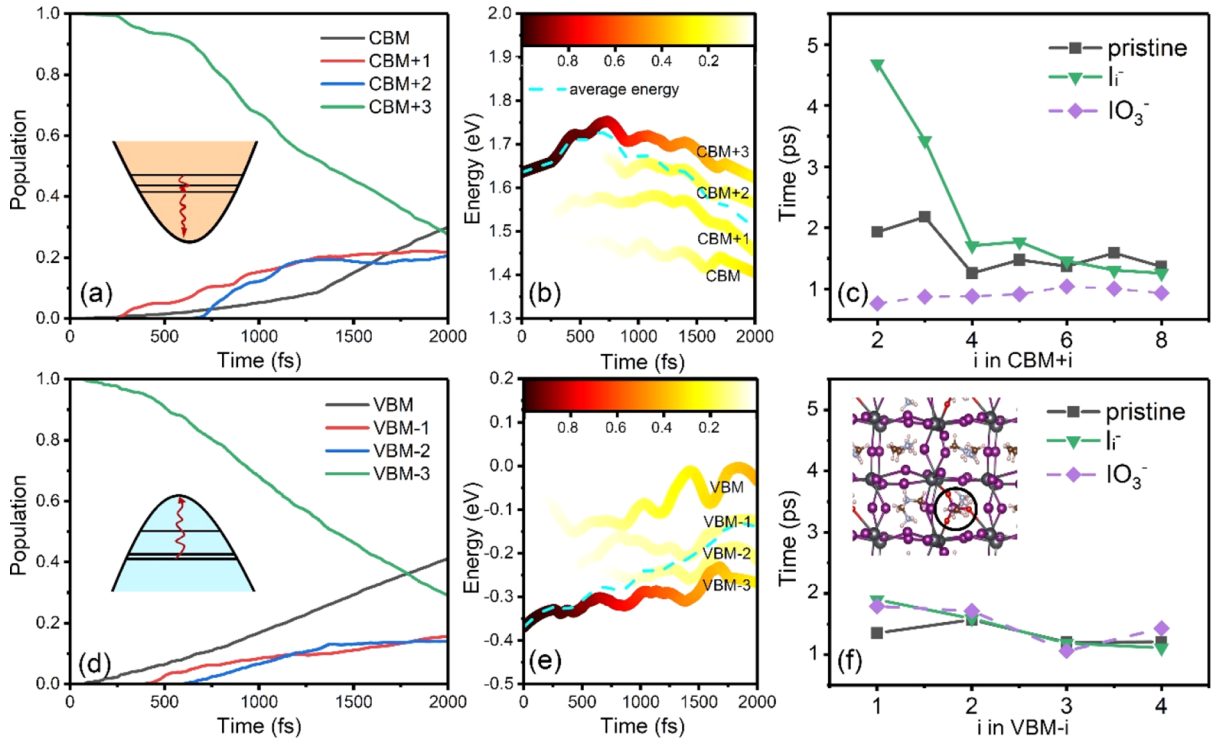

Figure 4. (a,d) Population of key states of hot electron and hot hole cooling for pristine $MAPbI_3$. The red curvy arrows in the insets represent the corresponding HC cooling dynamics pathways. (b,e) Time domain average energy relaxation of hot electron and hot hole in each state of pristine $MAPbI_3$. After 2 ps, the hot electron and hole lost 0.12 and 0.22 eV of energy, respectively. (c,f) HC cooling time of pristine, I_i^-, and IO_3^- systems. IO_3^-, marked in the inset of panel (f), significantly accelerates the hot electron cooling while having a negligible effect on hot hole cooling.

(below 100 cm^{-1}) compared with that in the pristine, MA_v^+, and I_v^- systems (top plane in Figure 3e). This lower frequency vibration mode creates the majority of NA e−ph coupling,[57] which originated from the heavy Pb and I atoms that have small nuclear velocities. Such small nuclear velocities tend to result in a small NAC value and, ultimately, slow down hot electron cooling.[48,49] The spectral density of the hot hole cooling process in the I_i^- system is dominated by two low-frequency peaks at 40.76 and 122.02 cm^{-1} (bottom panel in Figure 3e). These modes rationalize the reduced NAC of hot hole cooling and reveal its steady cooling rate, even when the energy difference between energy levels is small. Visualization of the corresponding vibration vectors is given in Figure S2. The modes contributing most to the HC cooling processes originate from thermal fluctuations of both the I−Pb inorganic lattice and the organic cations. In particular, $[PbI_6]^{4-}$ octahedron vibrations significantly participate in the HC cooling dynamics of the I_i^- system. This is consistent with the results of the Fourier transform and reveals that I_i^- induces the vibration mode with a weak e−ph interaction and thus has a positive effect on HC cooling.

As discussed above, the weak e−ph interaction induced by the specific defect significantly affects the HC cooling dynamics. Moreover, the hot electron exhibits a slower cooling rate than the hot hole in all systems, both pristine and defective (Figure 2). To understand this fact in more detail, the populations of the key states involved in HC cooling are shown in Figures 4 and S3. It is found that hot electron tends to relax from the initial CBM + 3 to the adjacent CBM + 2 or CBM + 1 and that the direct relaxation between CBM + 3 and CBM is less favorable. On the contrary, the major hot hole relaxation occurs directly from the initial VBM − 3 to VBM rather than through VBM − 2 or VBM − 1. This means that hot electrons can store more energy than hot holes during the cooling process. As a result, extracting hot electrons can be predicted to maximize the utilization of solar energy and improve the PCE of the perovskite. To further estimate the energy loss during the HC cooling process, the time evolution of the average energy of HCs and the populations on each key energy level for the four $MAPbI_3$ systems are shown in Figures 4b,e and S4. For pristine $MAPbI_3$, the energy of hot electron resides in CBM + 1 and CBM + 2 with an energy loss of 0.12 eV, whereas the energy associated with hot hole cooling is primarily distributed in the VBM with an energy loss of 0.22 eV within 2 ps. Meanwhile, the energy levels in the VB exhibit larger fluctuations in comparison with those in the CB. Such large oscillatory behavior also favors energy loss during the hot hole cooling due to the small energy gap between energy levels in VB at some moments. Consequently, we conclude that the hot electron and hole will cool along the band-by-band relaxation pathway and direct relaxation pathway, respectively, leading to a twice smaller energy loss for the former compared to that for the latter.

So far, we have demonstrated that the I_i^- defect works best for slowing down the hot electron cooling and enhancing the performance of perovskites. Previous work reports that O_2 will likely interact with the electron-rich I_i^- and form a thermodynamically stable IO_3^- species.[58] Here, we consider the effect of O_2 on the HC cooling dynamics and calculate the HC cooling time to further explore the performance of the I_i^- system exposed to O_2, as shown in Figures 4c,f and S5. After oxygen passivation, the hot hole cooling time of I_i^- has negligible change, while the hot electron cooling time decreases significantly and is even smaller than that of pristine

https://doi.org/10.1021/jacs.2c08487
J. Am. Chem. Soc. 2022, 144, 18126−18134

perovskite, revealing the detrimental effect of oxygen on suppressing hot electron cooling. The Fourier transform spectral densities of I_i^- and IO_3^- at CBM + 2 and VBM − 1 are shown in Figure S6 to reveal the effect of e−ph interaction on HC cooling dynamics. In the IO_3^- system, the dominant vibration modes for both hot electron and hot hole cooling show blue shifts, as compared to the I_i^- system. In particular, more peaks at higher frequencies appear in the hot electron cooling process. Such high-frequency phonon modes increase the e−ph interaction and HC relaxation probability. That is why the HC cooling dynamics are significantly accelerated after oxygen passivation. Therefore, we suggest that oxygen should be strongly avoided if I_i^- is utilized to improve the photovoltaic performance of hot electrons.

CONCLUSIONS

In summary, we have systematically investigated the influence of three common intrinsic point defects (MA_v^+, I_v^-, and I_i^-) on the HC cooling dynamics in LHPs by performing DFT and NAMD simulations. Our results show that only I_i^- efficiently slows down hot electron cooling by a factor of 1.5−2 and simultaneously avoids acceleration of hot hole cooling, revealing the defect-dependent HC cooling dynamics behavior in LHPs. This important phenomenon is primarily attributed to the favorable modulation of the synergism between the HC−phonon interaction and energy-level distribution upon introduction of I_i^-. Further, we demonstrate the band-by-band relaxation pathway for hot electrons and the direct relaxation pathway for hot holes, rationalizing the faster energy loss for hot hole cooling. In addition, the IO_3^- species formed by the interaction of oxygen and I_i^- induce high-frequency phonon modes participating in the hot electron cooling process and significantly decrease the hot electron relaxation time. In view of the practical synthesis of LHPs, we suggest that introducing interstitial point defects I_i^- while simultaneously avoiding oxygen can slow down HC cooling and decrease energy loss. Our simulations suggest a new strategy to slow down HC cooling in LHPs and will be of interest in designing novel HC photovoltaic devices.

COMPUTATIONAL DETAILS

In this work, the geometry optimization, static electronic structure, and ab initio molecular dynamics (AIMD) calculations were implemented through the Vienna Ab initio Simulation Package (VASP).[59,60] The exchange−correlation interaction was treated with the Perdew−Burke−Ernzerhof (PBE) functional in the framework of the generalized gradient approximation.[61] The projector-augmented wave method was adopted to describe the electron−ion interaction.[62] A kinetic cutoff of 500 eV and a Monkhorst−Pack 5 × 5 × 5 k-mesh grid were adopted for geometry optimization and electronic structure calculations. The lattice constants and atomic positions were fully relaxed until the atomic forces were smaller than 0.02 eV $Å^{-1}$. The electron relaxation convergence criterion was 10^{-5} eV. The weak van der Waals interaction was considered using the Grimme DFT-D3 method.[63]

The photoexcited HC cooling dynamics were modeled by NAMD simulations, implemented in the PYXAID code.[54,64] All the AIMD and NAMD calculations were carried out at the Γ point due to the expensive computational cost in a supercell with 96 atoms. After the geometry optimization, the relaxed structures were warmed up to 300 K during 2 ps in the canonical ensemble (NVT) through repeated velocity rescaling. Then, a 4 ps AIMD trajectory was generated in the microcanonical ensemble (NVE) with a time step of 1 fs, and the NAC elements were obtained from these trajectories. Two hundred initial configurations were selected randomly in the first 2 ps AIMD trajectory, and 3000 surface hopping trajectories were adopted for each chosen initial structure. Then, the photoexcited HC cooling dynamics simulations were carried out for 2 ps. More computational details are given in the Supporting Information.

Note that we do not employ a hybrid functional (HF) in the electronic structure calculations since HF always gives an energy gap much larger than the experimental values.[65] To obtain an accurate energy gap, HF should be combined with spin−orbit coupling (SOC) to cancel the band gap error.[66] However, HF calculations are too expensive to be used in the quantum dynamics simulations on systems of the current size, and SOC increases the computational cost further. In contrast, the PBE functional has been identified to give a good description of the electronic properties of $MAPbI_3$. The previous study has examined that the band gap and location of the trap state at the PBE level remain largely unchanged compared with those at the HSE06 + SOC level for $MAPbI_3$ with an antisite defect.[67] Therefore, to maintain computational efficiency, we use the PBE functional in the present work.

SOC is important in $MAPbI_3$ because of the strong relativistic effect of Pb. Considering the SOC effect in combination with the PBE functional will lead to underestimation of the band gap and generate a Rashba splitting in $MAPbI_3$.[68,69] However, the band gap value has little influence on the intraband relaxation of HCs. Similarly, the Rashba splitting tends to occur at the band edge, having little influence on HC relaxation. Therefore, SOC was not considered in our calculations.

ASSOCIATED CONTENT

Supporting Information

The Supporting Information is available free of charge at https://pubs.acs.org/doi/10.1021/jacs.2c08487.

Computational details; dominant vibration vectors, time domain average energy relaxation, and additional evolutions of state population during hot electron and hot hole relaxation in the pristine, MA_v^+, I_v^-, and I_i^- systems; and spectral densities of key states for the IO_3^- system (PDF)

AUTHOR INFORMATION

Corresponding Authors

Thomas Frauenheim − *Bremen Center for Computational Materials Science, University of Bremen, Bremen 28359, Germany; Beijing Computational Science Research Center, Beijing 100193, China; Shenzhen JL Computational Science and Applied Research Institute, Shenzhen 518109, China*; Email: thomas.frauenheim@bccms.uni-bremen.de

Oleg V. Prezhdo − *Departments of Chemistry, and Physics and Astronomy, University of Southern California, Los Angeles, California 90089, United States*; orcid.org/0000-0002-5140-7500; Email: prezhdo@usc.edu

Jinlan Wang − *School of Physics, Southeast University, Nanjing 211189, China*; orcid.org/0000-0002-4529-874X; Email: jlwang@seu.edu.cn

Authors

Zhaobo Zhou − *School of Physics, Southeast University, Nanjing 211189, China; Bremen Center for Computational Materials Science, University of Bremen, Bremen 28359, Germany;* orcid.org/0000-0003-2904-1845

Junjie He − *Bremen Center for Computational Materials Science, University of Bremen, Bremen 28359, Germany; Department of Physical and Macromolecular Chemistry, Faculty of Science, Charles University in Prague, Prague 12843, Czech Republic;* orcid.org/0000-0001-6447-7893

Complete contact information is available at: https://pubs.acs.org/10.1021/jacs.2c08487

Notes

The authors declare no competing financial interest.

■ ACKNOWLEDGMENTS

This work was supported by the National Key Research and Development Program of China (grant 2021YFA1200700), the Natural Science Foundation of China (grants 22033002, 21973011, and 22173019), and the DFG Research and Training Group RTG 2247 "Quantum Mechanical Materials Modelling". O.V.P. acknowledges the support of the US National Science Foundation (grant CHE-2154367). The authors thank the National Supercomputing Center of Tianjin and the Big Data Computing Center of Southeast University for providing the facility support on the calculations.

■ REFERENCES

(1) Pazos-Outón, L. M.; Szumilo, M.; Lamboll, R.; Richter, J. M.; Crespo-Quesada, M.; Abdi-Jalebi, M.; Beeson, H. J.; Vrućinić, M.; Alsari, M.; Snaith, H. J.; Ehrler, B.; Friend, R. H.; Deschler, F. Photon Recycling in Lead Iodide Perovskite Solar Cells. *Science* **2016**, *351*, 1430−1433.

(2) Blancon, J. C.; Tsai, H.; Nie, W.; Stoumpos, C. C.; Pedesseau, L.; Katan, C.; Kepenekian, M.; Soe, C. M. M.; Appavoo, K.; Sfeir, M. Y.; Tretiak, S.; Ajayan, P. M.; Kanatzidis, M. G.; Even, J.; Crochet, J. J.; Mohite, A. D. Extremely Efficient Internal Exciton Dissociation Through Edge States in Layered 2D Perovskites. *Science* **2017**, *355*, 1288−1292.

(3) Chen, B.; Baek, S.-W.; Hou, Y.; Aydin, E.; De Bastiani, M.; Scheffel, B.; Proppe, A.; Huang, Z.; Wei, M.; Wang, Y.-K.; Jung, E.-H.; Allen, T. G.; Van Kerschaver, E.; García de Arquer, F. P.; Saidaminov, M. I.; Hoogland, S.; De Wolf, S.; Sargent, E. H. Enhanced Optical Path and Electron Diffusion Length Enable High-Efficiency Perovskite Tandems. *Nat. Commun.* **2020**, *11*, 1257.

(4) Meggiolaro, D.; Motti, S. G.; Mosconi, E.; Barker, A. J.; Ball, J.; Andrea Riccardo Perini, C.; Deschler, F.; Petrozza, A.; De Angelis, F. Iodine Chemistry Determines the Defect Tolerance of Lead-Halide Perovskites. *Energy Environ. Sci.* **2018**, *11*, 702−713.

(5) National Renewable Energy Laboratory. Efficiency Chart. https://www.nrel.gov/pv/cell-efficiency.html (accessed Jun 30, 2022).

(6) Shockley, W.; Queisser, H. J. Detailed Balance Limit of Efficiency of p−n Junction Solar Cells. *J. Appl. Phys.* **1961**, *32*, 510−519.

(7) Ross, R. T.; Nozik, A. J. Efficiency of Hot-Carrier Solar Energy Converters. *J. Appl. Phys.* **1982**, *53*, 3813−3818.

(8) Nozik, A. J. Utilizing Hot Electrons. *Nat. Energy* **2018**, *3*, 170−171.

(9) Xing, G.; Mathews, N.; Sun, S.; Lim, S.; Lam, M.; Grätzel, M.; Mhaisalkar, S.; Sum, C. Long-Range Balanced Electron- and Hole-Transport Lengths in Organic-Inorganic $CH_3NH_3PbI_3$. *Science* **2013**, *342*, 344−347.

(10) Zhu, H.; Miyata, K.; Fu, Y.; Wang, J.; Joshi, P. P.; Niesner, D.; Williams, K. W.; Jin, S.; Zhu, X. Y. Screening in Crystalline Liquids Protects Energetic Carriers in Hybrid Perovskites. *Science* **2016**, *353*, 1409−1413.

(11) Guo, Z.; Wan, Y.; Yang, M.; Snaider, J.; Zhu, K.; Huang, L. Long-Range Hot-Carrier Transport in Hybrid Perovskites Visualized by Ultrafast Microscopy. *Science* **2017**, *356*, 59−62.

(12) Chen, J.; Messing, M. E.; Zheng, K.; Pullerits, T. Cation-Dependent Hot Carrier Cooling in Halide Perovskite Nanocrystals. *J. Am. Chem. Soc.* **2019**, *141*, 3532−3540.

(13) Yin, J.; Maity, P.; Naphade, R.; Cheng, B.; He, J. H.; Bakr, O. M.; Brédas, J. L.; Mohammed, O. F. Tuning Hot Carrier Cooling Dynamics by Dielectric Confinement in Two-Dimensional Hybrid Perovskite Crystals. *ACS Nano* **2019**, *13*, 12621−12629.

(14) Righetto, M.; Lim, S. S.; Giovanni, D.; Lim, J. W. M.; Zhang, Q.; Ramesh, S.; Tay, Y. K. E.; Sum, T. C. Hot Carriers Perspective on the Nature of Traps in Perovskites. *Nat. Commun.* **2020**, *11*, 2712.

(15) Yin, J.; Naphade, R.; Maity, P.; Gutiérrez-Arzaluz, L.; Almalawi, D.; Roqan, I. S.; Brédas, J. L.; Bakr, O. M.; Mohammed, O. F. Manipulation of Hot Carrier Cooling Dynamics in Two-Dimensional Dion-Jacobson Hybrid Perovskites via Rashba Band Splitting. *Nat. Commun.* **2021**, *12*, 3995.

(16) Li, M.; Bhaumik, S.; Goh, T. W.; Kumar, M. S.; Yantara, N.; Grätzel, M.; Mhaisalkar, S.; Mathews, N.; Sum, T. C. Slow Cooling and Highly Efficient Extraction of Hot Carriers in Colloidal Perovskite Nanocrystals. *Nat. Commun.* **2017**, *8*, 14350.

(17) Wang, T.; Jin, L.; Hidalgo, J.; Chu, W.; Snaider, J. M.; Deng, S.; Zhu, T.; Lai, B.; Prezhdo, O.; Correa-Baena, J. P.; Huang, L. Protecting Hot Carriers by Tuning Hybrid Perovskite Structures with Alkali Cations. *Sci. Adv.* **2020**, *6*, No. eabb1336.

(18) Joshi, P. P.; Maehrlein, S. F.; Zhu, X. Dynamic Screening and Slow Cooling of Hot Carriers in Lead Halide Perovskites. *Adv. Mater.* **2019**, *31*, 1803054.

(19) Miyata, K.; Meggiolaro, D.; Trinh, M. T.; Joshi, P. P.; Mosconi, E.; Jones, S. C.; De Angelis, F.; Zhu, X. Y. Large Polarons in Lead Halide Perovskites. *Sci. Adv.* **2017**, *3*, No. e1701217.

(20) Miyata, K.; Atallah, T. L.; Zhu, X. Y. Lead Halide Perovskites: Crystal-Liquid Duality, Phonon Glass Electron Crystals, and Large Polaron Formation. *Sci. Adv.* **2017**, *3*, No. e1701469.

(21) Yang, Y.; Ostrowski, D. P.; France, R. M.; Zhu, K.; van de Lagemaat, J.; Luther, J. M.; Beard, M. C. Observation of a Hot-Phonon Bottleneck in Lead-Iodide Perovskites. *Nat. Photonics* **2015**, *10*, 53−59.

(22) Fu, J.; Xu, Q.; Han, G.; Wu, B.; Huan, C. H. A.; Leek, M. L.; Sum, T. C. Hot Carrier Cooling Mechanisms in Halide Perovskites. *Nat. Commun.* **2017**, *8*, 1300.

(23) Mondal, N.; De, A.; Das, S.; Paul, S.; Samanta, A. Ultrafast Carrier Dynamics of Metal Halide Perovskite Nanocrystals and Perovskite-Composites. *Nanoscale* **2019**, *11*, 9796−9818.

(24) Madjet, M. E.; Berdiyorov, G. R.; El-Mellouhi, F.; Alharbi, F. H.; Akimov, A. V.; Kais, S. Cation Effect on Hot Carrier Cooling in Halide Perovskite Materials. *J. Phys. Chem. Lett.* **2017**, *8*, 4439−4445.

(25) Price, M. B.; Butkus, J.; Jellicoe, T. C.; Sadhanala, A.; Briane, A.; Halpert, J. E.; Broch, K.; Hodgkiss, J. M.; Friend, R. H.; Deschler, F. Hot-Carrier Cooling and Photoinduced Refractive Index Changes in Organic-Inorganic Lead Halide Perovskites. *Nat. Commun.* **2015**, *6*, 8420.

(26) Shen, Q.; Ripolles, T. S.; Even, J.; Ogomi, Y.; Nishinaka, K.; Izuishi, T.; Nakazawa, N.; Zhang, Y.; Ding, C.; Liu, F.; Toyoda, T.; Yoshino, K.; Minemoto, T.; Katayama, K.; Hayase, S. Slow Hot Carrier Cooling in Cesium Lead Iodide Perovskites. *Appl. Phys. Lett.* **2017**, *111*, 153903.

(27) Djurišić, A. B.; Liu, F.; Ng, A. M. C.; Dong, Q.; Wong, M. K.; Ng, A.; Surya, C. Stability Issues of the Next Generation Solar Cells. *Phys. Status Solidi RRL* **2016**, *10*, 281−299.

(28) Sherkar, T. S.; Momblona, C.; Gil-Escrig, L.; Ávila, J.; Sessolo, M.; Bolink, H. J.; Koster, L. J. A. Recombination in Perovskite Solar Cells: Significance of Grain Boundaries, Interface Traps, and Defect Ions. *ACS Energy Lett.* **2017**, *2*, 1214−1222.

(29) Wu, X.; Trinh, M. T.; Niesner, D.; Zhu, H.; Norman, Z.; Owen, J. S.; Yaffe, O.; Kudisch, B. J.; Zhu, X. Y. Trap States in Lead Iodide Perovskites. *J. Am. Chem. Soc.* **2015**, *137*, 2089−2096.
(30) Leijtens, T.; Eperon, G. E.; Barker, A. J.; Grancini, G.; Zhang, W.; Ball, J. M.; Kandada, A. R. S.; Snaith, H. J.; Petrozza, A. Carrier Trapping and Recombination: the Role of Defect Physics in Enhancing the Open Circuit Voltage of Metal Halide Perovskite Solar Cells. *Energy Environ. Sci.* **2016**, *9*, 3472−3481.
(31) Correa-Baena, J.-P.; Tress, W.; Domanski, K.; Anaraki, E. H.; Turren-Cruz, S.-H.; Roose, B.; Boix, P. P.; Grätzel, M.; Saliba, M.; Abate, A.; Hagfeldt, A. Identifying and Suppressing Interfacial Recombination to Achieve High Open-Circuit Voltage in Perovskite Solar Cells. *Energy Environ. Sci.* **2017**, *10*, 1207−1212.
(32) Leijtens, T.; Stranks, S. D.; Eperon, G. E.; Lindblad, R.; Johansson, E. M. J.; McPherson, I. J.; Rensmo, H.; Ball, J. M.; Lee, M. M.; Snaith, H. J. Electronic Properties of Meso-Superstructured and Planar Organometal Halide Perovskite Films: Charge Trapping, Photodoping, and Carrier Mobility. *ACS Nano* **2014**, *8*, 7147−7155.
(33) Johnston, M. B.; Herz, L. M. Hybrid Perovskites for Photovoltaics: Charge-Carrier Recombination, Diffusion, and Radiative Efficiencies. *Acc. Chem. Res.* **2016**, *49*, 146−154.
(34) Du, M. H. Efficient Carrier Transport in Halide Perovskites: Theoretical Perspectives. *J. Mater. Chem. A* **2014**, *2*, 9091−9098.
(35) Agiorgousis, M. L.; Sun, Y.-Y.; Zeng, H.; Zhang, S. Strong Covalency-Induced Recombination Centers in Perovskite Solar Cell Material $CH_3NH_3PbI_3$. *J. Am. Chem. Soc.* **2014**, *136*, 14570−14575.
(36) Yin, W. J.; Shi, T.; Yan, Y. Unique Properties of Halide Perovskites as Possible Origins of the Superior Solar Cell Performance. *Adv. Mater.* **2014**, *26*, 4653−4658.
(37) Shockley, W.; Read, W. T. Statistics of the Recombinations of Holes and Electrons. *Phys. Rev.* **1952**, *87*, 835−842.
(38) Li, M.; Fu, J.; Xu, Q.; Sum, T. C. Slow Hot-Carrier Cooling in Halide Perovskites: Prospects for Hot-Carrier Solar Cells. *Adv. Mater.* **2019**, *31*, No. e1802486.
(39) König, D.; Casalenuovo, K.; Takeda, Y.; Conibeer, G.; Guillemoles, J. F.; Patterson, R.; Huang, L. M.; Green, M. A. Hot Carrier Solar Cells: Principles, Materials and Design. *Phys. E* **2010**, *42*, 2862−2866.
(40) Bernardi, M.; Vigil-Fowler, D.; Lischner, J.; Neaton, J. B.; Louie, S. G. Ab Initio Study of Hot Carriers in the First Picosecond after Sunlight Absorption in Silicon. *Phys. Rev. Lett.* **2014**, *112*, 257402.
(41) Jhalani, V. A.; Zhou, J.-J.; Bernardi, M. Ultrafast Hot Carrier Dynamics in GaN and Its Impact on the Efficiency Droop. *Nano Lett.* **2017**, *17*, 5012−5019.
(42) Tong, X.; Bernardi, M. Toward Precise Simulations of the Coupled Ultrafast Dynamics of Electrons and Atomic Vibrations in Materials. *Phys. Rev. Res.* **2021**, *3*, 023072.
(43) Zhou, Z.; Ju, M.-G.; Wang, J. Rational Unraveling of Alkali Metal Concentration-Dependent Photovoltaic Performance of Halide Perovskites: Octahedron Distortion vs Surface Reconstruction. *J. Phys. Chem. Lett.* **2022**, *13*, 362−370.
(44) Hyeon-Deuk, K.; Prezhdo, O. V. Multiple Exciton Generation and Recombination Dynamics in Small Si and CdSe Quantum Dots: An Ab Initio Time-Domain Study. *ACS Nano* **2012**, *6*, 1239−1250.
(45) Trivedi, D. J.; Wang, L.; Prezhdo, O. V. Auger-Mediated Electron Relaxation Is Robust to Deep Hole Traps: Time-Domain Ab Initio Study of CdSe Quantum Dots. *Nano Lett.* **2015**, *15*, 2086−2091.
(46) Pal, S.; Casanova, D.; Prezhdo, O. V. Effect of Aspect Ratio on Multiparticle Auger Recombination in Single-Walled Carbon Nanotubes: Time Domain Atomistic Simulation. *Nano Lett.* **2018**, *18*, 58−63.
(47) Zhou, G.; Lu, G.; Prezhdo, O. V. Modeling Auger Processes with Nonadiabatic Molecular Dynamics. *Nano Lett.* **2021**, *21*, 756−761.
(48) Chu, W.; Saidi, W. A.; Zhao, J.; Prezhdo, O. V. Soft Lattice and Defect Covalency Rationalize Tolerance of b-$CsPbI_3$ Perovskite Solar Cells to Native Defects. *Angew. Chem., Int. Ed.* **2020**, *59*, 6435−6441.
(49) Chu, W.; Zheng, Q.; Prezhdo, O. V.; Zhao, J.; Saidi, W. A. Low-Frequency Lattice Phonons in Halide Perovskites Explain High Defect Tolerance toward Electron-Hole Recombination. *Sci. Adv.* **2020**, *6*, No. eaaw7453.
(50) Zhou, G.; Chu, W.; Prezhdo, O. V. Structural Deformation Controls Charge Losses in $MAPbI_3$: Unsupervised Machine Learning of Nonadiabatic Molecular Dynamics. *ACS Energy Lett.* **2020**, *5*, 1930−1938.
(51) Guo, R.; Wang, S. Anion-Dependent Hot Carrier Dynamics in Chalcogenide Perovskites $SrSnX_3$ (X = S, Se). *J. Phys. Chem. C* **2018**, *123*, 29−35.
(52) Zheng, Q.; Chu, W.; Zhao, C.; Zhang, L.; Guo, H.; Wang, Y.; Jiang, X.; Zhao, J. Ab Initio Nonadiabatic Molecular Dynamics Investigations on the Excited Carriers in Condensed Matter Systems. *Wiley Interdiscip. Rev. Comput. Mol. Sci.* **2019**, *9*, No. e1411.
(53) Zhou, Z.; Zhang, Y.; Zhang, X.; Niu, X.; Wu, G.; Wang, J. Suppressing Photoexcited Electron-Hole Recombination in $MoSe_2$/WSe_2 Lateral Heterostructures via Interface-Coupled State Engineering: a Time-Domain Ab Initio Study. *J. Mater. Chem. A* **2020**, *8*, 20621−20628.
(54) Akimov, A. V.; Prezhdo, O. V. Advanced Capabilities of the PYXAID Program: Integration Schemes, Decoherence Effects, Multiexcitonic States, and Field-Matter Interaction. *J. Chem. Theory Comput.* **2014**, *10*, 789−804.
(55) Leguy, A. M. A.; Goñi, A. R.; Frost, J. M.; Skelton, J.; Brivio, F.; Rodríguez-Martínez, X.; Weber, O. J.; Pallipurath, A.; Alonso, M. I.; Campoy-Quiles, M.; Weller, M. T.; Nelson, J.; Walsh, A.; Barnes, P. R. F. Dynamic Disorder, Phonon Lifetimes, and the Assignment of Modes to the Vibrational Spectra of Methylammonium Lead Halide Perovskites. *Phys. Chem. Chem. Phys.* **2016**, *18*, 27051−27066.
(56) Quarti, C.; Grancini, G.; Mosconi, E.; Bruno, P.; Ball, J. M.; Lee, M. M.; Snaith, H. J.; Petrozza, A.; De Angelis, F. The Raman Spectrum of the $CH_3NH_3PbI_3$ Hybrid Perovskite: Interplay of Theory and Experiment. *J. Phys. Chem. Lett.* **2014**, *5*, 279−284.
(57) He, J. L.; Fang, W. H.; Long, R. Unravelling the Effects of Oxidation State of Interstitial Iodine and Oxygen Passivation on Charge Trapping and Recombination in $CH_3NH_3PbI_3$ Perovskite: a Time-Domain Ab Initio Study. *Chem. Sci.* **2019**, *10*, 10079−10088.
(58) Meggiolaro, D.; Mosconi, E.; De Angelis, F. Mechanism of Reversible Trap Passivation by Molecular Oxygen in Lead-Halide Perovskites. *ACS Energy Lett.* **2017**, *2*, 2794−2798.
(59) Kresse, G.; Furthmüller, J. Efficiency of Ab-Initio Total Energy Calculations for Metals and Semiconductors Using a Plane-Wave Basis Set. *Comput. Mater. Sci.* **1996**, *6*, 15−50.
(60) Kresse, G.; Furthmüller, J. Efficient Iterative Schemes for Ab Initio Total-Energy Calculations Using a Plane-Wave Basis Set. *Phys. Rev. B: Condens. Matter Mater. Phys.* **1996**, *54*, 11169−11186.
(61) Perdew, J. P.; Burke, K.; Ernzerhof, M. Generalized Gradient Approximation Made Simple. *Phys. Rev. Lett.* **1996**, *77*, 3865−3868.
(62) Kresse, G.; Joubert, D. From Ultrasoft Pseudopotentials to the Projector Augmented-Wave Method. *Phys. Rev. B: Condens. Matter Mater. Phys.* **1999**, *59*, 1758−1775.
(63) Grimme, S.; Antony, J.; Ehrlich, S.; Krieg, H. A Consistent and Accurate Ab Initio Parametrization of Density Functional Dispersion Correction (DFT-D) for the 94 Elements H-Pu. *J. Chem. Phys.* **2010**, *132*, 154104.
(64) Akimov, A. V.; Prezhdo, O. V. The PYXAID Program for Non-Adiabatic Molecular Dynamics in Condensed Matter Systems. *J. Chem. Theory Comput.* **2013**, *9*, 4959−4972.
(65) Quarti, C.; Mosconi, E.; Ball, J. M.; D'Innocenzo, V.; Tao, C.; Pathak, S.; Snaith, H. J.; Petrozza, A.; De Angelis, F. Structural and Optical Properties of Methylammonium Lead Iodide across the Tetragonal to Cubic Phase Transition: Implications for Perovskite Solar Cells. *Energy Environ. Sci.* **2016**, *9*, 155−163.
(66) Leguy, A. M. A.; Azarhoosh, P.; Alonso, M. I.; Campoy-Quiles, M.; Weber, O. J.; Yao, J.; Bryant, D.; Weller, M. T.; Nelson, J.; Walsh, A.; van Schilfgaarde, M.; Barnes, P. R. F. Experimental and Theoretical Optical Properties of Methylammonium Lead Halide Perovskites. *Nanoscale* **2016**, *8*, 6317−6327.

https://doi.org/10.1021/jacs.2c08487
J. Am. Chem. Soc. 2022, 144, 18126−18134

(67) Qiao, L.; Fang, W. H.; Long, R.; Prezhdo, O. V. Atomic Model for Alkali Metal Passivation of Point Defects at Perovskite Grain Boundaries. *ACS Energy Lett.* **2020**, *5*, 3813−3820.
(68) Li, W.; Zhou, L.; Prezhdo, O. V.; Akimov, A. V. Spin-Orbit Interactions Greatly Accelerate Nonradiative Dynamics in Lead Halide Perovskites. *ACS Energy Lett.* **2018**, *3*, 2159−2166.
(69) Frohna, K.; Deshpande, T.; Harter, J.; Peng, W.; Barker, B. A.; Neaton, J. B.; Louie, S. G.; Bakr, O. M.; Hsieh, D.; Bernardi, M. Inversion Symmetry and Bulk Rashba Effect in Methylammonium Lead Iodide Perovskite Single Crystals. *Nat. Commun.* **2018**, *9*, 1829.

https://doi.org/10.1021/jacs.2c08487
J. Am. Chem. Soc. 2022, 144, 18126−18134